ACS NANO

www.acsnano.org

ARTICLE

Coupling Curvature and Hydrophobicity: A Counterintuitive Strategy for Efficient Electroreduction of Nitrate into Ammonia

Jianan Gao, Qingquan Ma, Yihan Zhang, Shan Xue, Joshua Young, Mengqiang Zhao, Zhiyong Jason Ren, Jae-Hong Kim, and Wen Zhang*

Cite This: *ACS Nano* 2024, 18, 10302−10311

Read Online

ACCESS | Metrics & More | Article Recommendations | Supporting Information

ABSTRACT: **The electrochemical upcycling of nitrate (NO_3^-) to ammonia (NH_3) holds promise for synergizing both wastewater treatment and NH_3 synthesis. Efficient stripping of gaseous products (NH_3, H_2, and N_2) from electrocatalysts is crucial for continuous and stable electrochemical reactions. This study evaluated a layered electrocatalyst structure using copper (Cu) dendrites to enable a high curvature and hydrophobicity and achieve a stratified liquid contact at the gas−liquid interface of the electrocatalyst layer. As such, gaseous product desorption or displacement from electrocatalysts was enhanced due to the separation of a wetted reaction zone and a nonwetted zone for gas transfer. Consequently, this electrocatalyst structure yielded a 2.9-fold boost in per-active-site activity compared with that with a low curvature and high hydrophilic counterpart. Moreover, a NH_3 Faradaic efficiency of 90.9 ± 2.3% was achieved with nearly 100% NO_3^- conversion. This high-curvature hydrophobic Cu dendrite was further integrated with a gas-extraction membrane, which demonstrated a comparable NH_3 yield from the real reverse osmosis retentate brine.**

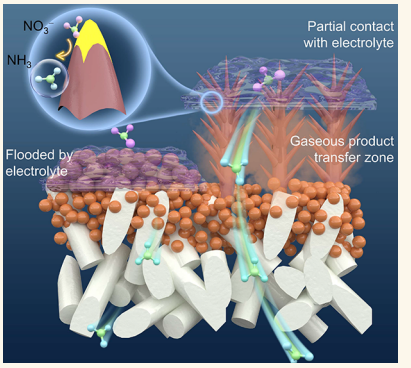

KEYWORDS: *electrochemical nitrate reduction, ammonia production, microenvironment, mass transfer, hierarchically structured dendrites, nanoarray*

1. INTRODUCTION

Ammonia (NH_3) is an essential commodity chemical used in fertilizer production, chemical synthesis, and liquid energy storage.[1,2] Currently, ammonia is mainly produced by the Haber−Bosch process, with a worldwide production of 170 million tons per year.[3] This production accounts for 1.4% of global carbon dioxide (CO_2) emission, emitting an equivalent of 2.9 tons of CO_2 per ton of NH_3 produced.[4] The produced ammonia ultimately ends up in nature as nitrogenous pollutants. Recovering nitrogen from agricultural wastewater or contaminated groundwater in the form of reusable NH_3 would alleviate environmental concerns by completing the nitrogen cycle. Electrochemical conversion of nitrate (NO_3^-) to NH_3 via the eight-electron nitrate reduction reaction (NO_3RR) is increasingly studied for sustainable ammonia synthesis.[5−9] Various electrocatalysts such as copper-, nickel-, ruthenium-, cobalt-, and titanium-based transition metal materials have been explored for NO_3RR.[10,11]

NO_3RR encounters two major limitations: insufficient active site binding with and charge transfer to NO_3^- and sluggish desorption of finial products from the active sites.[12−14] One approach to address this challenge is to enhance the activity and density of active sites of electrocatalysts through morphological optimization, elemental doping, metal (alloy) core−shell configurations, and single-atom catalyst formulations.[15−26] Alternative strategies involved the use of porous materials and electric fields to enhance the chemisorption of NO_3^- onto the active sites.[3,27] The NO_3RR consumes protons and therefore causes a high cathodic interfacial pH (*e.g.*, up to 11 under a current density of 5 mA cm^{-2}).[28−30] The rapid production of gaseous products such as NH_3, N_2, and H_2 at the cathode surface could lead to potential accumulation and electrode surface coverage by evolving bubbles, which could further hinder the mass transfer of NO_3^- toward the electrocatalytic reactions[31] and NH_3 production.[32] Therefore, redesigning the electrocatalyst layer structure to enhance both NO_3RR and gas separation is critical.

Received: February 10, 2024
Revised: March 16, 2024
Accepted: March 25, 2024
Published: March 27, 2024

Downloaded via NEW JERSEY INST OF TECHNOLOGY on July 4, 2024 at 23:00:05 (UTC).
See https://pubs.acs.org/sharingguidelines for options on how to legitimately share published articles.

ACS Publications

© 2024 American Chemical Society

https://doi.org/10.1021/acsnano.4c02020
ACS Nano 2024, 18, 10302−10311

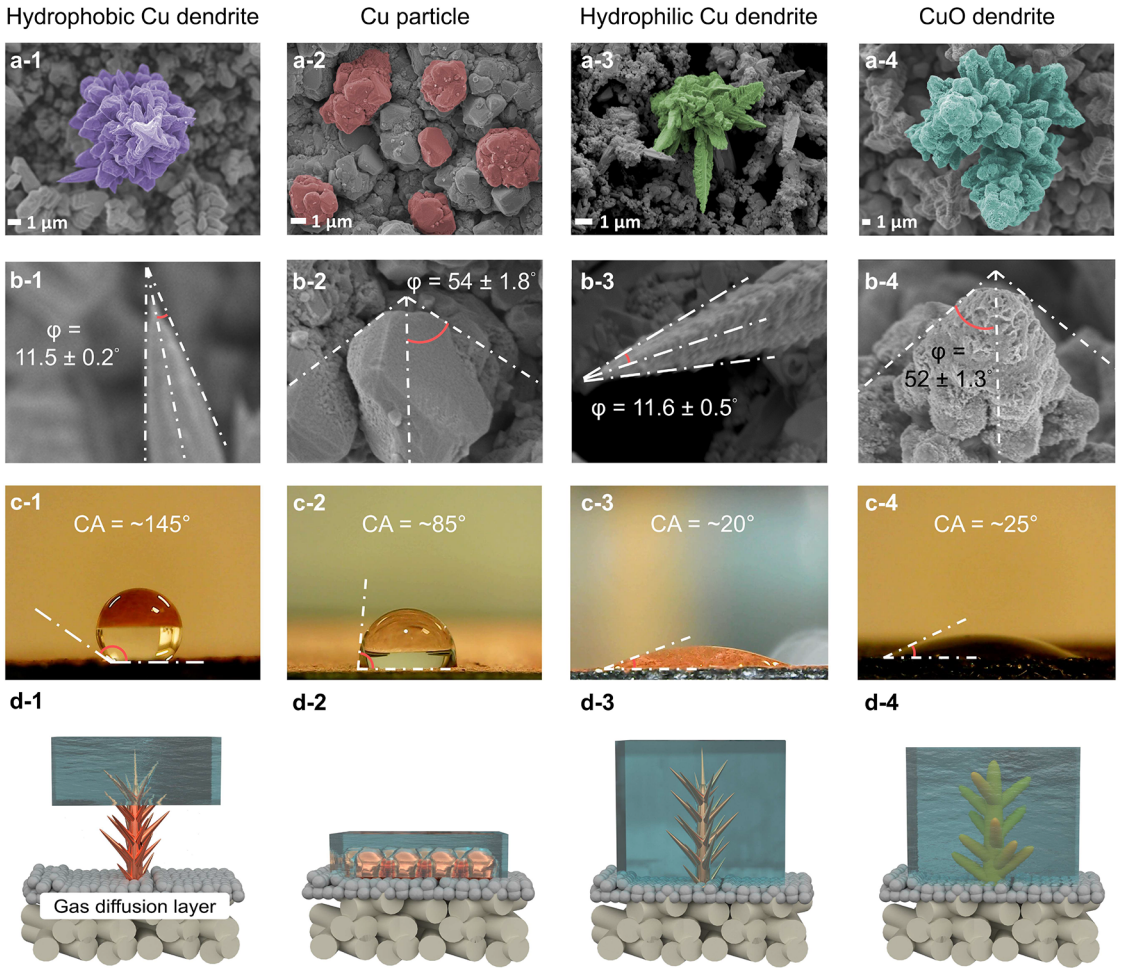

Figure 1. (a1-a4) Typical SEM images for the morphology of four electrocatalyst layers. (b1−b4) Typical SEM images for the apex half angle ϕ values of four electrocatalyst layers. (c1−c4) CAs measured with the electrolyte (10 mM NO_3^- and 0.1 M Na_2SO_4) on various electrocatalyst layers. (d1−d4) Illustrations of the guessed contact interfaces between different electrocatalyst layers and electrolyte based on CA values.

Electrocatalysts are typically expected to exhibit hydrophilicity to effectively interact with NO_3^- in the aqueous phase. In contrast, surface hydrophobicity can also be beneficial to spontaneously trap gas molecules produced at the electrocatalyst−electrolyte boundary[33] and to facilitate the separation of bubbles from the catalyst active sites. Highly curved surface structures (e.g., sharp nano tips) made of metals can create a positive Laplace pressure, making smooth surfaces superhydrophobic while maintaining local hydrophilicity.[34−36] Such structures also intensify thermal and electric fields at the tips by accumulating charges.[12,37−41] The locally enhanced fields not only attract reactants but also modulate reaction pathways, which potentially improve both the activity and selectivity of catalytic processes.[42,43] Hence, we hypothesize that a hydrophobic electrocatalyst surface layer with high curvatures (e.g., a dendrite structure with spiky or protruding sharp surfaces) can both boost the NO_3RR and reduce gas bubble accumulation at the electrocatalyst-electrolyte interface.

Considering the high activity of copper (Cu) toward NO_3RR,[3] we fabricated four Cu-based model electrocatalysts with different levels of curvatures and hydrophobicity. We assessed the impacts of curvature and hydrophobicity on the Faradaic efficiency and the production yield of NH_3. Density functional theory (DFT) calculations were further conducted to assess the effect of the tip-enhanced electric and thermal fields on the Gibbs free energies (ΔG) of the key intermediate (*NO−*NOH) conversion and the nitrate-to-ammonia pathway. The hydrophobic Cu dendrite electrocatalyst with the highest NO_3RR efficiency was screened and further integrated onto a gas extraction membrane for simultaneous NO_3RR and NH_3 recovery. The relevant performances were evaluated with both synthetic wastewater and real reverse osmosis (RO) retentate to gauge the practicality of this gas-evolving electrochemical system.

2. RESULTS AND DISCUSSION

2.1. Preparation and Characterizations of Cu-Based Electrocatalysts. Four kinds of Cu-based model electrocatalysts with different curvatures and hydrophobicities were prepared following the procedure described in the Experimental Section. Scanning electron microscopy (SEM) images in Figure 1a1−a4 and apex half angle (φ) analysis in Figure 1b1−b4 and a Figure S1 (Supporting Information) suggest that the first two catalysts, hydrophobic Cu dendrite (φ = 11.5 ± 0.2°) and hydrophilic Cu dendrite (φ = 11.6 ± 0.5°) exhibit a morphology of needle-leaved tree with sharp tips. The third catalyst, Cu particles (φ = 54 ± 1.8°), are obtuse-angled particulates. And the last one, CuO dendrite, also appears as a

https://doi.org/10.1021/acsnano.4c02020
ACS Nano 2024, 18, 10302−10311

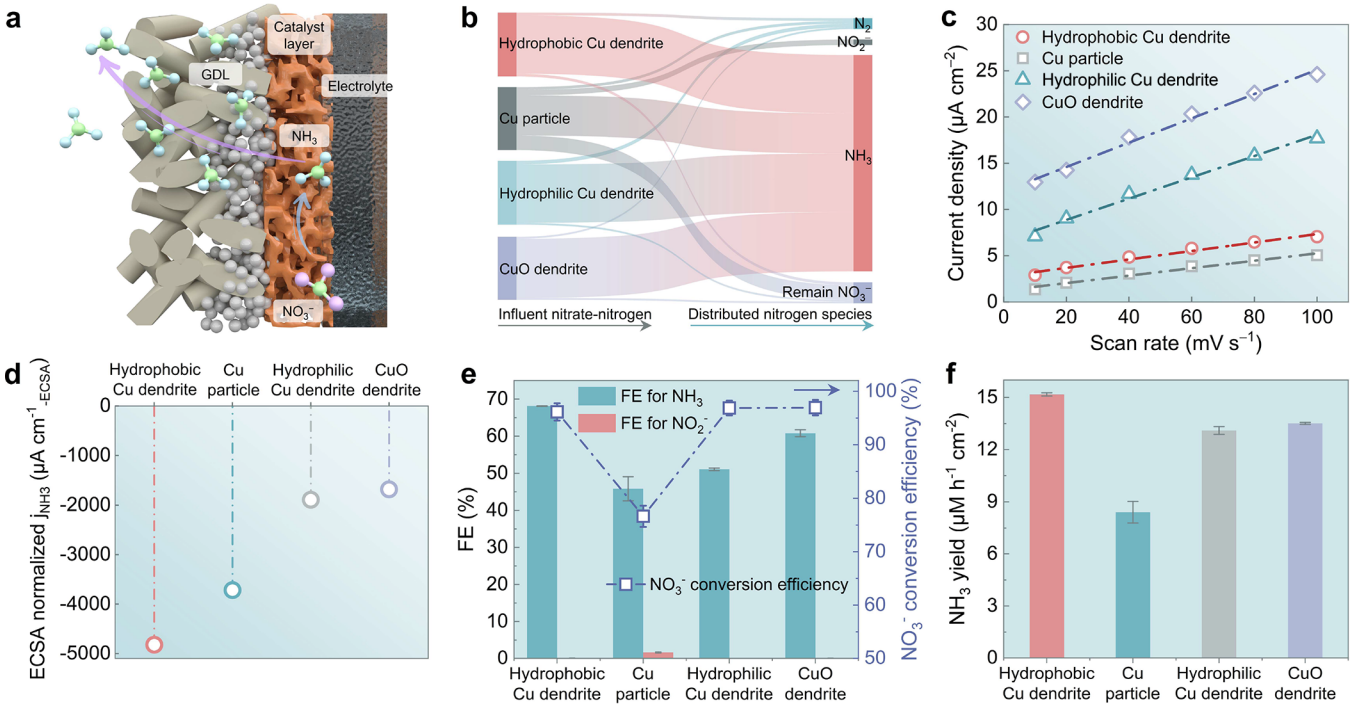

Figure 2. Electrocatalytic NO_3RR performance. (a) Illustration of regulation of gaseous product migration direction within the electrocatalyst layer. (b) Distributions of nitrogen species under the same nitrogen input conditions on different electrocatalyst layers. (c) Calculation of C_{dl} based on the current values (I_a and I_c) and the scan rate. (d) Comparison of ECSA normalized partial current density (j_{NH_3}) of different electrocatalyst layers under the same testing conditions. (e) FE for NH_3 and NO_2^- under different NO_3^- conversion efficiencies of different catalyst layers. (f) NH_3 yield rate of different catalyst layers. The calculation was based on the NH_3 separated from the electrolyte. Testing conditions are shown in Experimental Section (NO_3^- concentration, 10 mM; pH, ~7.0; supporting electrolyte, 0.1 M Na_2SO_4; cathodic potential, −1.20 V vs SHE; reaction time, 3.0 h per cycle).

needle-leaved tree with obtuse tips ($\varphi = 52 \pm 1.3°$). The water contact angles (CA) shown in Figure 1c1−c4 indicate that the surface with obtuse-angled catalysts, Cu particle and CuO dendrite, was relatively hydrophilic. In contrast, the surface with hydrophobic Cu dendrites was most hydrophobic with a CA of 145°. Note that the hydrophilic Cu dendrite showed strong hydrophilicity (CA = 20°). The enhanced surface roughness of the hydrophilic Cu dendrite, in contrast to the smooth surface of hydrophobic Cu dendrite, significantly boosts its wetting properties and hydrophilicity.[44] The X-ray diffractograms in Figure S2 confirm that the hydrophobic Cu dendrite, Cu particle, and hydrophilic Cu dendrite mainly consist of metallic Cu with the same major exposed crystal planes of (111) and (200), whereas the CuO dendrite has a single crystal plane of (002). These four catalysts, as illustrated in Figure 1d1−d4, are expected to have different liquid contacts and thus should elicit different NO_3RR activities. Additionally, the effect of Cu-valence states (Cu^{2+}, Cu^+, and Cu^0) and the vertical hierarchical structure may also play roles in mass transport and reactivity.

2.2. Catalytic Activity of Electrocatalyst Layers. We loaded the above copper-based catalysts onto a gas diffusion layer (GDL) as a cathodic membrane in a flow-type electrolyzer, as shown in Figure S3 (Supporting Information). This electrolyzer was intended to mitigate the detrimental effect of bubbles on the cathode that could impede NO_3^- ion transport in the electrolyte.[32,45] A synthetic wastewater containing 10 mM NO_3^- was introduced into the catholyte channel facing the catalyst layer of the membrane cathode. Simultaneously, a separate Na_2SO_4 electrolyte was pumped into the trap channel, facing the other side of this gas-permeable cathode to strip and capture the produced NH_3. This electrolyte was further directed to the anolyte channel to be acidified ($2H_2O \rightarrow O_2 + 4H^+ + 4e^-$; the relationship of cathodic/anodic interfacial pH and response current density is shown in Figure S4 (Supporting Information)) and reused for consecutive NH_3 capture, which is illustrated by Figures 2a and Figure S5 (Supporting Information).

First, the results in Figure 2b and Figure S6 (Supporting Information) confirmed that all four electrocatalysts produced NH_3 as the main end product in NO_3RR. The NH_3 selectivity was in the order of CuO dendrite (96.5 ± 2.0%) > hydrophobic Cu dendrite (95.2 ± 1.9%) > hydrophilic Cu dendrite (94.4 ± 1.9%) > Cu particle (82.0 ± 2.1%). Nitrite (NO_2^-) was barely detected in the catholyte, and the selectivity toward NO_2^- was as low as 0.7 ± 0.1%, except for Cu particle (11.7 ± 0.6%). Note that the initial concentration of NO_3^- in the feed was kept low at 10 mM, to compare the performance of various electrocatalyst layers under a constrained mass transfer condition for NO_3RR.

Considering the disparities in wettability across the different catalyst layers, we then evaluated their electrochemically active surface areas (ECSAs), which represent the portion of the catalyst in contact with, and thus accessible to, the electrolyte.[46] Figure 2c and Figure S7 (Supporting Information) show the CV curves of the four electrocatalyst layers. The electrochemical double-layer capacity (C_{dl}) was calculated based on the scan rate and the current values (I_a and I_c) and summarized in Table S1 (Supporting Information). The CuO dendrite and hydrophilic Cu dendrite exhibited the relatively

https://doi.org/10.1021/acsnano.4c02020
ACS Nano 2024, 18, 10302−10311

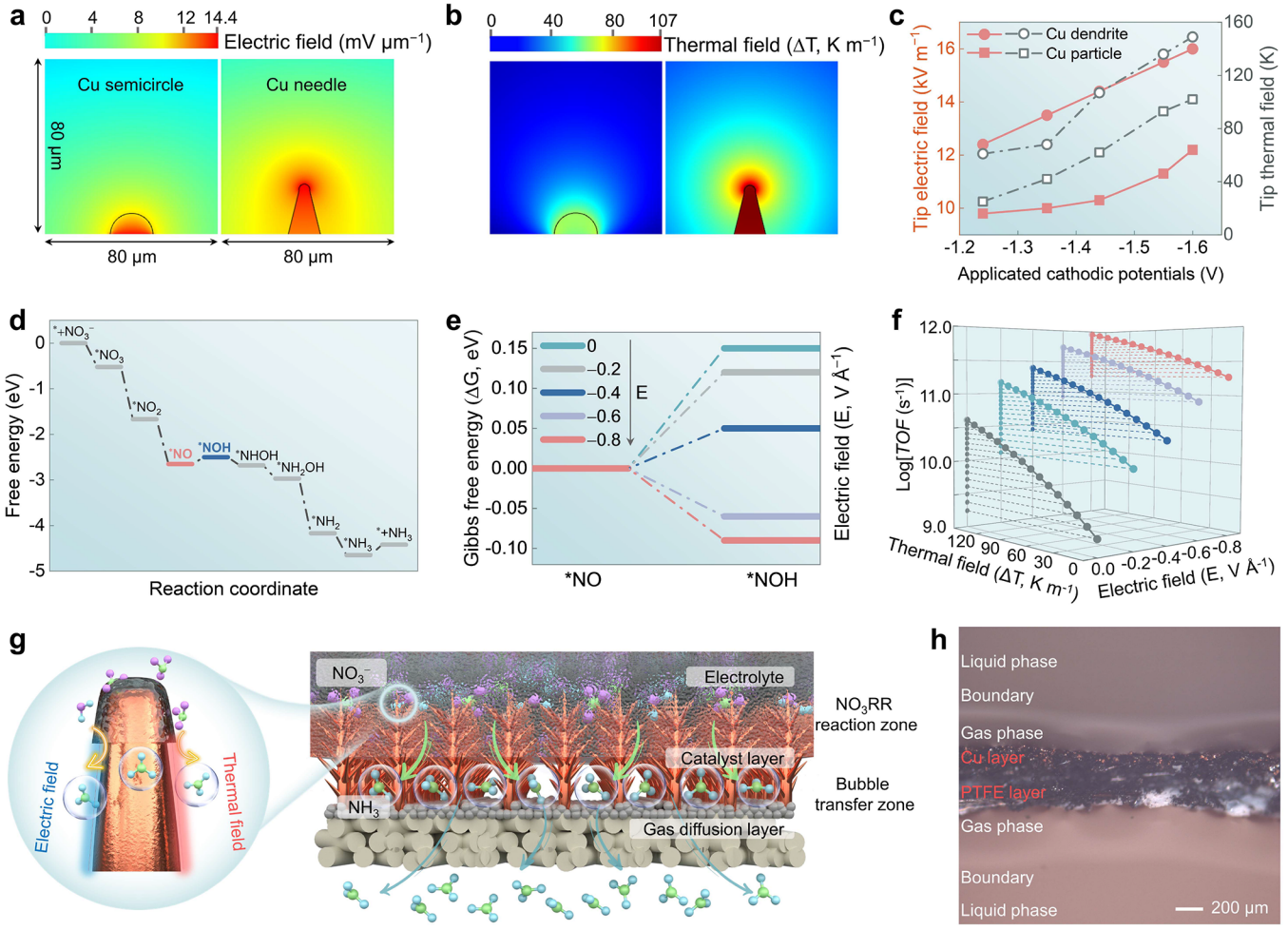

Figure 3. COMSOL and DFT simulations. (a) Electric field distribution on the Cu particle (left) and the single needle of the Cu dendrite (right). (b) Thermal field distribution on the Cu particle (left) and the single needle of the Cu dendrite (right). The thermal field (Δ*T*, K) is the temperature enhancement versus room temperature (298 K). (c) Electric field and thermal field at the Cu dendrite and Cu particle tips as a function of applied cathodic potentials. (d) Free energy and reaction pathways for corresponding intermediates during NO_3^- to NH_3 conversion on Cu (111). (e) Reaction Gibbs free energy diagrams of the hydrogenation process of *NO to *NOH on the Cu (111) surface under different electric fields. (f) TOF trend of *NO to *NOH conversion at various electric and thermal fields. (g) Demonstration diagram of the hydrophobic Cu dendrite electrocatalyst layer interface that partially contacts with the electrolyte and tip enhanced electric field and thermal field. (h) Cross section view of the hydrophobic Cu dendrite gas extraction membrane when immersed in electrolyte (10 mM NO_3^- and 0.1 M Na_2SO_4).

larger ECSA values of 2.19 cm^2_{ECSA} $cm^{-2}_{geometric}$ and 1.92 cm^2_{ECSA} $cm^{-2}_{geometric}$, attributable to the low water contact angle. The ESCA values of hydrophobic Cu dendrite and Cu particles were 0.76 cm^2_{ECSA} $cm^{-2}_{geometric}$ and 0.67 cm^2_{ECSA} $cm^{-2}_{geometric}$, respectively. Next, we normalized partial current density for NH_3 synthesis (j_{NH_3}, the response current only caused by total NH_3 yield, see the Experimental Section for details) based on ECSA. Results shown in Figure 2d reveal that the ECSA-normalized j_{NH_3} followed the trend of hydrophobic Cu dendrite (−4820 μA cm^{-1}_{ECSA}) > Cu particle (−3716 μA cm^{-1}_{ECSA}) > hydrophilic Cu dendrite (−1892 μA cm^{-1}_{ECSA}) > CuO dendrite (−1682 μA cm^{-1}_{ECSA}). Figure 2e illustrates that FE for NH_3 was in the order of hydrophobic Cu dendrite (68.1 ± 0.1%) > CuO dendrite (60.8 ± 0.9%) > hydrophilic Cu dendrite (51.1 ± 0.4%) > Cu particle (45.8 ± 3.2%). Finally, Figure 2f compares the NH_3 yield rates (calculated based on the captured NH_3 in the trap tank), which are in the order of hydrophobic Cu dendrite (15.2 ± 0.1 μM cm^{-2} h^{-1}) > CuO dendrite (13.5 ± 0.1 μM cm^{-2} h^{-1}) > hydrophilic Cu dendrite (13.1 ± 0.2 μM cm^{-2} h^{-1}) > Cu particle (8.4 ± 0.3 μM cm^{-2} h^{-1}).

Apparently, hydrophobic Cu dendrite achieved (1) the highest NH_3 production activity on a per active site basis with j_{NH3} of −4820 μA cm^{-1}_{ECSA}, (2) the highest FE for NH_3 of 68.1 ± 0.1%, and (3) the highest NH_3 yield rate of 15.2 ± 0.1 μM cm^{-2} h^{-1}. We speculate that hydrophobic Cu dendrite's curvature-enhanced hydrophobicity may have created a partial contact interface between the electrolyte and catalyst layer, which could efficiently separate reaction and gas-transfer zones and thus yielded a superior NH_3 yield. In contrast, a hydrophilic Cu dendrite with weaker hydrophobicity than a hydrophobic Cu dendrite would not efficiently expel locally produced gaseous products or bubbles from the electrocatalyst and thus compromise NO_3RR. The Cu particle's hydrophilic surface lacks high curvature induced thermal-electric fields, which will be discussed in detail in the following section, and thus may be oversaturated by electrolyte, which may also hinder NO_3RR and product migration. The CuO dendrite exhibits a similar vertical hierarchical structure compared with

https://doi.org/10.1021/acsnano.4c02020
ACS Nano 2024, 18, 10302−10311

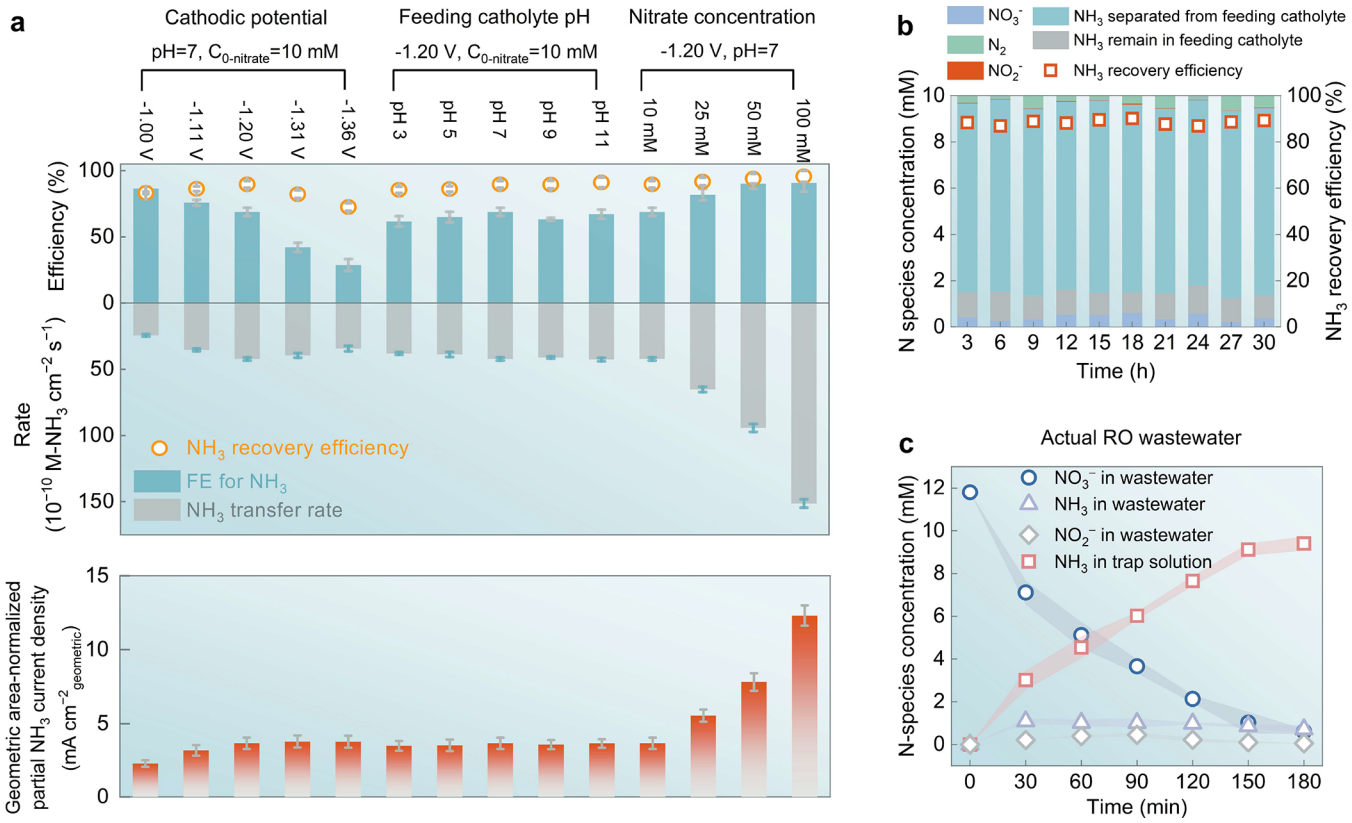

Figure 4. Practical ammonia product synthesis. (a) NH_3 recovery efficiency, FE for NH_3 production, NH_3 transfer rate, and geometric area normalized partial NH_3 current density of hydrophobic Cu dendrite gas extraction membrane at different cathodic potentials (−1.00 to −1.36 V vs SHE), feed catholyte pHs (~3.0−11.0), and nitrate concentrations (10−100 mM). (b) Stability test of the hydrophobic Cu dendrite gas extraction membrane at a constant cathodic potential of −1.20 V vs SHE. Testing conditions: feed catholyte pH 7.0, NO_3^- concentration 10 mM, supporting electrolyte 0.1 M Na_2SO_4, reaction time 3.0 h per cycle. (c) Evolution of N-species concentration for actual RO wastewater under a cathodic potential of −1.20 V vs SHE.

hydrophobic Cu dendrite. A negative potential will induce the *in situ* electrochemical conversion of Cu^{2+} into Cu^+ and Cu^0.[47] Compared with pure metallic Cu^0 in hydrophobic Cu dendrite, the mixed-Cu-valence states of CuO dendrite were reported to exhibit enhanced NO_3RR performance.[29,48] The observed lower NH_3 yield associated with the CuO dendrite can be attributed to its hydrophilic obtuse tips. The slow release of bubbles within the electrolyte-flooded electrocatalyst layer likely impedes the mass transfer of the NO_3^- ions to the active sites.

We recognize that the above electrocatalysts may still not outcompete with some top-tier catalysts (e.g., Cu nanoparticles encapsulated with a porous carbon framework[3]) when treating a similar low NO_3^- concentration (*e.g.*, our reported FE is approximately 20% lower than the highest). The primary objective behind comparing various materials was to furnish insights for the catalytic layer's design strategy rather than maximizing FE, which could be achieved by many approaches such as raising the electrolyte pH with KOH to mitigate the side reactions such as hydrogen evolution. Instead, our results mainly suggest the electrocatalyst layer's curvature structures (a smaller φ) and surface hydrophobicity have a profound influence on NO_3RR activity.

2.3. Mechanistic Analysis of Performance Improvement. We performed finite element method (FEM) based simulations and density functional theory (DFT) calculations to understand mechanisms that contribute to the enhanced NO_3RR activity of the hydrophobic Cu dendrite. First, FEM simulations compared the electric field and thermal field distribution of hydrophobic Cu dendrite and Cu particle under a cathodic potential of −1.20 V vs SHE. Table S2 summarizes the major parameters used in this simulation. Figure 3a,b reveals that the sharp end of the hydrophobic Cu dendrite exhibits enhanced local electrostatic and thermal field strength (14.4 mV μm^{-1} and 107 K m^{-1}). However, the Cu particle demonstrates a much lower local electrostatic field of ~10 mV μm^{-1} and thermal field (~52 K m^{-1}). Electric and thermal fields on the hydrophobic Cu dendrite were consistently higher than those on the Cu particle at different cathodic potentials from −1.00 V vs SHE to −1.36 V vs SHE as compared in Figure 3c and Figure S8 (Supporting Information).

We further employed DFT to understand how this locally enhanced electric field at the catalyst tips affected the NO_3RR. The free energy of intermediates during the transition from NO_3^- to NH_3 was calculated on the Cu (111) surface, a dominant exposed facet according to the XRD analysis. The reaction pathway in Figure 3d identified *NO to *NOH hydrogenation as an endothermic rate-limiting step (Figure S9 (Supporting Information)).[17,28,49] When the electric field increased from 0 to −0.8 V $Å^{-1}$, the free energy for this hydrogenation process decreased (Figure 3e), accompanied by a decrease of activation energy (ΔE_a) as shown in Table S3 (Supporting Information). Figure 3f and Figure S10 (Supporting Information) indicate that turnover frequency (TOF) for the *NO to *NOH conversion also increased by nearly 2 orders of magnitude with the increasing electric and

https://doi.org/10.1021/acsnano.4c02020
ACS Nano 2024, 18, 10302−10311

thermal fields. These simulation results collectively suggest that local intensification of the electric field at the catalyst's sharp tips may enhance NO_3RR kinetics.

Figure 3g further illustrates how the hydrophobic Cu dendrite electrocatalyst layer may benefit from the enhanced electric field and thermal fields at the catalyst tip and synergistically boost NH_3 production. Similar synergy has also been reported in other electrocatalytic processes such as proton reduction for the hydrogen evolution reaction (HER),[50] CO_2 reduction,[38] and electroporation of bacteria for disinfection.[51] Upon immersion in the electrolyte, a gas layer was notably present on the surface of the hydrophobic Cu dendrite layer, as shown in Figure S11 in the Supporting Information. Conversely, the hydrophilic Cu dendrite layer was flooded by the electrolyte. To provide unequivocal visual confirmation of the catalyst layer's interaction with the liquid, we examined the microscale gas−liquid interface more closely. For the hydrophobic Cu dendrite, distinct boundaries between the liquid and gas phases were visible on both the hydrophobic Cu dendrite and the PTFE layer sides, illustrated in Figure 3h. For the hydrophilic Cu dendrite, the liquid−gas phase boundary was solely observed on the PTFE layer side, as detailed in Figure S12 (Supporting Information). Droplets of electrolyte on the hydrophilic Cu dendrite layer were absorbed within 3 s (Figure S13 (Supporting Information)), whereas on the hydrophobic Cu dendrite layer, stability was maintained for over 200 s. Upon the application of a −1.20 V vs SHE cathodic potential, bubble formation was initiated on the hydrophobic Cu dendrite layer and subsequently migrated toward the PTFE layer side, as opposed to dispersing into the electrolyte (Figure S14 (Supporting Information)). This phenomenon of bubble formation on the reverse side of the hydrophobic Cu dendrite gas extraction electrode (i.e., back of membrane module) during the NO_3^--to-NH_3 conversion experiment aligns with the aforementioned observations and further supports the efficacy of gas removal from the electrocatalytic layer, as visualized in Figure S15 (Supporting Information). Thus, we present the presence of a hydrophilic reaction zone at the tip of the hydrophobic Cu dendrite and a hydrophobic transfer zone facing gas transfer layer, a similar Cassie−Baxter state, where an air shell forms in the vicinity between liquid and solid surface.[52] This phenomenon is posited to mitigate the obstruction of gaseous products within the electrocatalytic stratum.[32] At the gas−liquid−solid interface, the gas bubble detachment from catalyst may cause transient turbulences near the bubble trajectory, which may further enhance the NO_3^- mass transfer to the active reaction sites of the catalyst.[53] Thus, the hydrophobic Cu dendrite's morphological features explain its superior NH_3 recovery efficiency, when compared to the other three catalysts with similar NH_3 yields in Figure S16 (Supporting Information).

2.4. Evaluation of NO_3RR on this Hydrophobic Cu Dendrite Membrane Platform. We expanded our investigation of the hydrophobic Cu dendrite to evaluate its NO_3RR performance under a wide range of conditions that represent various ammonia production scenarios. We first varied the cathodic potential (Figure 4a and Figure S17 (Supporting Information)). As the cathodic potential increased, the FE for NH_3 decreased from 86.6 ± 1.3% to 28.8 ± 4.4%. Besides, the NH_3 recovery rate and efficiency all exhibited a volcano curve, where they reached the highest levels of $(47.1 \pm 1.7) \times 10^{-10}$ M-NH_3 cm^{-2} s^{-1} and 88.3 ± 2.8%, respectively, when the cathodic potential was −1.20 V vs SHE. The geometric area normalized partial NH_3 current density increased by 1.6-fold with the cathodic potential increased from −1.00 to −1.20 V vs SHE and remained stable around 3.7 ± 0.4 to 3.8 ± 0.4 mA cm^{-2}.

We also varied the feed solution pH from 3 to 11 to represent diverse wastewater types such as acidic phosphate fertilizer industry wastewater (pH 2−3)[54] and alkaline wastewater from uranium extraction and ion-exchange resin regeneration (pH 9−11).[55] This hydrophobic Cu dendrite gas extraction membrane performance was not affected by the pH variations (Figure 4a and Figures S18 and S19 (Supporting Information)). This is because the cathodic interfacial pH could quickly remain in the range of 11.0−11.5,[28] even at a minimal response current density of 5 mA cm^{-2} under a −1.20 V vs SHE cathodic potential, even when the feed pH varied from 3.0 to 11.0.

Next, we changed the initial NO_3^- concentration from 10 mM (typical for most wastewater[56]) to 100 mM, a high level for brine wastewater from ion exchange or RO processes.[57] As the NO_3^- concentration increased from 10 to 100 mM, the FE for NH_3 increased from 68.9 ± 3.1% to 90.9 ± 6.8%. Meanwhile, the NH_3 transfer rate also increased from $(42.1 \pm 1.2) \times 10^{-10}$ to $(151.4 \pm 3.1) \times 10^{-10}$ M-NH_3 cm^{-2} s^{-1}, which caused a rise in the NH_3 yield rate from $(47.1 \pm 1.7) \times 10^{-10}$ to $(159.5 \pm 3.4) \times 10^{-10}$ M-NH_3 cm^{-2} s^{-1} and the geometric area normalized partial NH_3 current density from 3.7 ± 0.4 to 12.3 ± 0.7 mA cm^{-2}. In addition to the improved cathodic reaction kinetics pertaining to the NO_3RR, we also observed the increase in NH_3 recovery efficiency from 88.3 ± 2.8% to 94.9 ± 4.6%. Clearly, a high NO_3^- concentration also suppressed the generation of gaseous byproducts like H_2, which otherwise would compete for the gas diffusion pathways in the cathodic membrane, potentially impeding NH_3 transport. A similar phenomenon was also observed when increasing the cathodic potential from −1.20 V vs SHE to −1.36 V vs SHE. Under similar j_{NH_3} (−3.7 to −3.8 mA cm^{-2}), the NH_3 FE decreased from 68.9 ± 3.1% to 28.8 ± 4.4%, resulting in declined NH_3 recovery efficiencies from 88.3 ± 2.8% to 69.7 ± 3.1%.

We further performed ten consecutive cycles of electrolysis to assess the stability of the hydrophobic Cu dendrite layer. The electrolyte was replaced after each 3 h cycle when ∼95% NO_3^-−N conversion efficiency and ∼90% NH_3 recovery efficiency were achieved. We observed a stable NH_3 yield rate, NO_3^- conversion efficiency, and NH_3 recovery efficiency over a 30 h electrolysis at the cathodic potential of −1.20 V vs SHE (Figure 4b). This stability is attributed to the surface feature of hydrophobicity for the Cu dendrite electrocatalyst layer that prevents wetting and enables efficient gas product diversion under a tip-induced thermal-electric field.[58] Besides, the SEM analysis and contact angle test revealed that the dendritic morphology of the top catalyst surface and hydrophobicity were well preserved after the 30 h electrolysis test (Figure S20 (Supporting Information)).

Finally, to validate the practical applicability, we performed a test using real RO retentate obtained from the Yuma Desalting Plant in Arizona. This wastewater contains an average concentration of NO_3^- of approximately 11.8 mM with other major parameters shown in Table S4 (Supporting Information). Figure 4c shows the NO_3^- conversion efficiency of 94.8 ± 1.2% and NH_3 recovery efficiency of 91.7 ± 1.5%, which match well with the results we obtained with the

https://doi.org/10.1021/acsnano.4c02020
ACS Nano 2024, 18, 10302−10311

synthetic NO_3^- wastewater. Nevertheless, a relatively high cathodic potential of −1.20 V vs SHE and a high pH near the cathodic membrane could induce transition metal reduction and metal precipitation in the form of carbonates and hydroxides. To avoid potential cathode passivation, strategies such as pulsed electrolysis[59] and a periodic polarity swap between cathode and anode[60] have been suggested previously.

3. CONCLUSIONS

Our study demonstrates that electrocatalyst layers characterized by high curvature and pronounced hydrophobicity can enhance the yield rate and FE of NH_3 during NO_3RR. This enhancement is ascribed to the solid−liquid interface that facilitates bubble separation within the electrocatalyst layer and consequently enhances NO_3^- mass transfer from the liquid phase to the catalyst. Moreover, the high curvature structure amplifies the local electric-thermal fields and reduces the energy barrier for *NO hydrogenation to *NOH, a rate-limiting step in the NO_3RR pathway. This presented structural design may also be used toward diverse catalytic materials for other aqueous electrocatalytic transformations with bubble generation, such as hydrogen/oxygen evolution reactions.

4. EXPERIMENTAL SECTION

4.1. Preparation of Gas Extraction Membrane Electrodes with Different Copper-Based Catalyst Layers. *4.1.1. Synthesis of Hydrophobic Cu Dendrite and CuO Dendrite.* The different copper-based catalyst layers were all directly electrodeposited on the AvCarb GDS2230 gas-diffusion substrate purchased from the Fuel Cell Store. To improve the hydrophobicity and mechanical strength of the gas-diffusion substrate, the carbon fiber side of the gas-diffusion substrate was coated with PTFE at a surface coverage of 1 ± 0.05 mg cm^{-2} using a 10 wt % PTFE solution diluted from a Teflon PTFE DISP 30 Fluoropolymer Dispersion. The PTFE-coated gas-diffusion substrate was calcined in a muffle furnace at 270 °C for 10 min. The hydrophobic Cu dendrite thin film was obtained in an electrodeposition process by applying a constant negative potential (−0.502 V vs SHE) using a CH Instruments 700E Potentiostat. The electrodeposition process was carried out in a H-cell, which was separated by a proton exchange membrane (PEM) (Nafion 117, Dupont). A three-electrode configuration was constructed with the pretreated gas-diffusion electrode substrate (an exposed area: 3 cm × 3 cm), an IrO_2−RuO_2/Ti electrode (an exposed area: 3 cm × 3 cm), and a saturated calomel electrode (SCE, +0.241 V vs SHE) as the working electrode, counter electrode, and reference electrode, respectively. To improve the substrate surface wettability and the electrodeposition repeatability, the gas-diffusion substrate was treated with isopropyl alcohol prior to catalyst deposition. The plating bath was a 0.1 M $CuSO_4{\cdot}5H_2O$ solution in deionized water with pH of 2 (adjusted by 1 M H_2SO_4). The counter electrode chamber was filled with 0.1 M Na_2SO_4 solution. Electrodeposition was conducted as described above for 700 s to result in a catalyst loading of 2.3 ± 0.1 mg cm^{-2} as determined above. The obtained electrocatalyst layer, namely hydrophobic Cu dendrite, was rinsed with DI water and then dried in a 50 °C vacuum for 5 h. The CuO dendrite was obtained by calcinating the hydrophobic Cu dendrite at 350 °C for 30 min.

4.1.2. Synthesis of Hydrophilic Cu Dendrite. The hydrophilic Cu dendrite was synthesized using an electrodeposition method identical with that of the hydrophobic Cu dendrite, with a different plating solution (0.1 M $CuCl_2$ and 0.1 M Na_2SO_4 solution) and a different potential (−0.759 V vs SHE for 450 s), resulting in a catalyst loading equivalent to that of the hydrophobic Cu dendrite.

4.1.3. Synthesis of Cu Particle. The Cu particle was synthesized using an electrodeposition method identical to that of the hydrophobic Cu dendrite, with a different potential (−0.201 V vs SHE for 1000 s), resulting in a catalyst loading equivalent to that of the hydrophobic Cu dendrite.

4.2. Characterization of the Electrocatalysts and Gas Extraction Membranes. The JSM-7900F field emission scanning electron microscope (FE-SEM) (JEOL, Japan) with coupled EDS was used to analyze the morphology and chemical compositions of different copper-based catalyst layers. The X-ray powder diffractometer (XRD) was taken on Philips, EMPYREAN, and PANalytical Almelo with Co Kα radiation (λ = 1.789 Å) to investigate the crystalline structures. The X-ray photoelectron spectroscope (XPS, Thermo, K-Alpha, USA) with monochromatic Al Kα radiation ($h\nu$ = 1486.6 eV) was employed to measure the surficial chemical states and compositions. The binding energy of C 1s (284.8 eV) was used as a reference to calibrate the spectra. The liquid−gas boundary at the gas extraction membrane interface and bubble generation/transport behavior were observed by a Carl Zeiss Axitoech 100 HD model microscope.

4.3. Electrochemical Measurements of the Electrocatalyst Layers. To investigate the electrochemical double-layer capacity (EDLC, C_{dl}) of the different Cu catalyst layers, cyclic voltammetry (CV) tests were performed in a three-electrode H-type cell with a CH Instruments 700E Potentiostat. The H-cell was separated by a proton exchange membrane (Nafion 117, Dupont). The gas extraction electrode with different Cu catalyst layers, a IrO_2−RuO_2/Ti plate, and SCE served as the working electrode, counter electrode, and reference electrode, respectively. The response current intensity of CV tests was recorded within a potential range of ±0.05 V around open-circuit potential (OCP), where only double-layer charging and discharging occurs (no Faradaic process), at scan rates (ν) of 10−100 mV s^{-1}.[46] The double-layer capacitance was regarded as the indicator of active site number, which was the slope of the linear regression by plotting the charging current of the double layer (I_a and I_c) versus the CV scan rate in eq 1.[61] The ECSA was subsequently calculated by comparing the capacitance of the nanostructured surfaces against that of a flat Cu surface with an area of 1 cm^2.

$$\frac{I_a - I_c}{2} = C_{dl}\nu \tag{1}$$

4.4. Electrochemical Flow-Cell Component, Assembly, and Operation. The flow cell was comprised of three channels: anolyte, catholyte and NH_3 trap, as depicted in Figure 1a and Figure S3 (Supporting Information). The anolyte channel (dimensions 30 mm × 30 mm; 5 mm long) contained the IrO_2−RuO_2/Ti anode (1 mm thickness). The catholyte channel (dimensions 30 mm × 30 mm; 5 mm long) contained the electrode with different copper-based catalyst layers as the cathode. The anolyte and catholyte channels were separated by a proton exchange membrane (Nafion 117, Dupont). The NH_3 trap channel (30 mm × 30 mm; 5 mm long) was used to capture the NH_3 extracted from the catholyte via the electrode. The catholyte and NH_3 trap channels were separated by the cathode. The copper-based catalyst side of the cathode faced the catholyte channel, while the PTFE gas diffusion layer faced the NH_3 trap channel. Silicone gaskets with a 30 mm × 30 mm window were placed between each layer to achieve sufficient sealing. Each channel has an inlet and outlet (4 mm OD; 2 mm ID) to pump the electrolyte into and out of the channel.

To promote mixing and minimize the diffusion boundary layer, the fluid inside the three channels was recirculated by two peristaltic pumps (MASTERFLEX L/S) at a flow rate of 25 mL min^{-1}. The electrolyte solution (50 mL, 0.1 M Na_2SO_4, pH 7) was recirculated among the trap channel, anode channel, and trap tank. The synthetic wastewater (50 mL, 10−100 mM NO_3^-, 0.1 M Na_2SO_4, pH 3−11) or actual RO wastewater was recirculated between the cathode channel and the feed tank. The cathodic potential was controlled to be −1.00 to −1.36 V vs SHE with a response current density range of ∼2−15 mA cm^{-2}.

4.5. Performance Evaluation of the Electrocatalytic NO_3^- Reduction to NH_3. The nitrate, nitrite, and ammonia concentrations in the feed and trap tanks were all measured by ultraviolet−visible (UV−vis) spectrophotometry as detailed in the Supporting Information.[15]

https://doi.org/10.1021/acsnano.4c02020
ACS Nano 2024, 18, 10302−10311

The selectivity (S_{NH_3}, %) and Faradaic efficiency (FE, %) for NH_3 were calculated by

$$S_{NH_3}\,(\%) = \frac{\Delta[C_{NH_3}]}{\Delta[C_{NO_3^-}]} \times 100 \tag{2}$$

$$\mathrm{FE}\,(\%) = \frac{n \times F \times N_i}{Q} \times 100 \tag{3}$$

The partial current density toward ammonia production (j_{NH_3}) is the product of FE for NH_3 production and the total response current density (I_{Total}), which was further normalized to geometric surface areas ($cm^{-2}_{geometric}$) and/or ECSA (mA cm^2_{ECSA})

$$j_{NH_3} = \mathrm{FE}\,(\%) \times I_{\mathrm{Total}} \tag{4}$$

where $\Delta[C_{NH_3}]$ and $\Delta[C_{NO_3^-}]$ are the concentration difference of NH_3 (the sum concentration in feed tank and trap tank) and NO_3^- (the concentration in feed tank) before and after the operation of this electrochemical flow-cell, n is the electron transfer number (8) per mole of reduced nitrate to NH_3, N_i is the amount (mol) of the produced NH_3, and Q is the total charge (C) passing the electrode, which was calculated based on the integration of the curve I (A) vs t (s).

The NH_3 yield rate ($\mu M\ h^{-1}\ cm^{-2}$) and NH_3 transfer rate (M-NH_3 $cm^{-2}\ s^{-1}$) were obtained by

$$\mathrm{NH_3\ yield\ rate} = \frac{\text{generated NH}_3\text{ concentration}}{t \times S} \tag{5}$$

$$\mathrm{NH_3\ transfer\ rate} = \frac{n_{NH_3}}{t \times S} \tag{6}$$

where n_{NH_3} is the moles of NH_3 passing through the gas exchange membrane per unit time, t is the unit time (h or s), and S is the size of the gas exchange membrane (cm^2).

The NH_3 recovery efficiency (%) was calculated by

$$\mathrm{NH_3\ recovery}\,(\%) = \frac{\text{NH}_3\text{ in trap tank}}{\text{total generated NH}_3} \times 100 \tag{7}$$

4.6. Calculation of TOF. Calculations were extended to include activation energy (ΔE_a) and turnover frequency (TOF) for a comprehensive kinetic evaluation of the *NO to *NOH conversion.[37,62]

$$\mathrm{TOF} = \frac{kT}{h} \times \exp\left(-\frac{\Delta E_a}{kT}\right) \tag{8}$$

The equation relates k, the Boltzmann constant (8.617×10^{-5} eV K^{-1}), and h, the Planck constant (4.136×10^{-15} eV Hz^{-1}), to T, the temperature in Kelvin, and ΔE_a, the activation energy for the *NO−*NOH transition.

4.7. Simulation and Computational Methods. Detailed simulation and computational methods, including core metadata and formula development, are described in the Supporting Information. In general, the Finite Element Method (FEM) simulations were performed by COMSOL Multiphysics version 6.1 as a stationary, 2D axisymmetric model consisting of an electrolyte diffusion layer and a Cu needle/semicircle. The FEM simulation was constructed on the "Electric Currents" module and the "Heat Transfer in Solids and Fluids" module. Density functional theory (DFT) calculations were performed using the Perdew−Burke−Ernzerhof functional, as implemented in the Vienna Ab initio Simulation Package.

ASSOCIATED CONTENT

Supporting Information

The Supporting Information is available free of charge at https://pubs.acs.org/doi/10.1021/acsnano.4c02020.

Physicochemical characterization (including apex half angle ϕ and XRD), physical installation diagram and setup of the continuous electrochemical reaction flow cell, cathodic/anodic interfacial pH calculation, and figure, detailed N-species evolution over time and electrochemical tests (CV tests and ECSA calculation table) of different electrolyte layers, operating method and data for COMSOL and DFT simulations, actual pictures of air bubbles extracted from the working membrane module, detailed N-species evolution over time of different cathodic potentials, electrolyte pHs, and nitrate concentrations, water chemistry of actual RO retentate, and detection method of nitrate, nitrite, and ammonia (PDF)

AUTHOR INFORMATION

Corresponding Author

Wen Zhang − *Department of Civil and Environmental Engineering, New Jersey Institute of Technology, Newark, New Jersey 07102, United States; Department of Chemical & Materials Engineering, New Jersey Institute of Technology, Newark, New Jersey 07102, United States;* orcid.org/0000-0001-8413-0598; Email: wen.zhang@njit.edu

Authors

Jianan Gao − *Department of Civil and Environmental Engineering, New Jersey Institute of Technology, Newark, New Jersey 07102, United States;* orcid.org/0000-0003-1255-1240

Qingquan Ma − *Department of Civil and Environmental Engineering, New Jersey Institute of Technology, Newark, New Jersey 07102, United States;* orcid.org/0000-0001-6879-6410

Yihan Zhang − *Department of Civil and Environmental Engineering, New Jersey Institute of Technology, Newark, New Jersey 07102, United States*

Shan Xue − *Department of Civil and Environmental Engineering, New Jersey Institute of Technology, Newark, New Jersey 07102, United States*

Joshua Young − *Department of Chemical & Materials Engineering, New Jersey Institute of Technology, Newark, New Jersey 07102, United States*

Mengqiang Zhao − *Department of Chemical & Materials Engineering, New Jersey Institute of Technology, Newark, New Jersey 07102, United States*

Zhiyong Jason Ren − *Department of Civil and Environmental Engineering and the Andlinger Center for Energy and the Environment, Princeton University, Princeton, New Jersey 08544, United States;* orcid.org/0000-0001-7606-0331

Jae-Hong Kim − *Department of Chemical and Environmental Engineering, Yale University, New Haven, Connecticut 06520, United States;* orcid.org/0000-0003-2224-3516

Complete contact information is available at: https://pubs.acs.org/10.1021/acsnano.4c02020

Author Contributions

J.G. conceived the project, designed/performed the experiment, and wrote the original draft. Q.M. and J.Y. conducted the COMSOL and DFT calculations. Y.Z. contributed to the SEM characterization. S.X. and M.Z. provided assistance in describing the hydrophobic/hydrophilic properties. W.Z.,

https://doi.org/10.1021/acsnano.4c02020
ACS Nano 2024, 18, 10302−10311

Z.J.R., and J.-H.K. were responsible for supervision, conceptualization, writing, reviewing, and editing.

Notes

The authors declare no competing financial interest.

ACKNOWLEDGMENTS

The study was financially supported by the NSF/BSF project (award number: 2215387) and New Jersey Water Resources Research Institute (award number: G21AP10595-01). We extend our gratitude to Md Mohidul Alam Sabuj for his invaluable assistance with the interface and bubble behavior experiments.

REFERENCES

(1) Chen, J. G.; Crooks, R. M.; Seefeldt, L. C.; Bren, K. L.; Bullock, R. M.; Darensbourg, M. Y.; Holland, P. L.; Hoffman, B.; Janik, M. J.; Jones, A. K.; Kanatzidis, M. G.; King, P.; Lancaster, K. M.; Lymar, S. V.; Pfromm, P.; Schneider, W. F.; Schrock, R. R. Beyond fossil fuel-driven nitrogen transformations. *Science* **2018**, *360*, No. eaar6611.

(2) MacFarlane, D. R.; Cherepanov, P. V.; Choi, J.; Suryanto, B. H. R.; Hodgetts, R. Y.; Bakker, J. M.; Ferrero Vallana, F. M.; Simonov, A. N. A Roadmap to the Ammonia Economy. *Joule* **2020**, *4*, 1186−1205.

(3) Song, Z.; Liu, Y.; Zhong, Y.; Guo, Q.; Zeng, J.; Geng, Z. Efficient Electroreduction of Nitrate into Ammonia at Ultralow Concentrations Via an Enrichment Effect. *Adv. Mater.* **2022**, *34*, 2204306.

(4) Guo, J.; Chen, P. Ammonia history in the making. *Nature Catalysis* **2021**, *4*, 734−735.

(5) Rosca, V.; Duca, M.; de Groot, M. T.; Koper, M. T. M. Nitrogen Cycle Electrocatalysis. *Chem. Rev.* **2009**, *109*, 2209−2244.

(6) Kani, N. C.; Nguyen, N. H. L.; Markel, K.; Bhawnani, R. R.; Shindel, B.; Sharma, K.; Kim, S.; Dravid, V. P.; Berry, V.; Gauthier, J. A.; Singh, M. R. Electrochemical Reduction of Nitrates on CoO Nanoclusters-Functionalized Graphene with Highest Mass Activity and Nearly 100% Selectivity to Ammonia. *Adv. Energy Mater.* **2023**, *13*, 2204236.

(7) Daiyan, R.; Tran-Phu, T.; Kumar, P.; Iputera, K.; Tong, Z.; Leverett, J.; Khan, M. H. A.; Asghar Esmailpour, A.; Jalili, A.; Lim, M.; Tricoli, A.; Liu, R.-S.; Lu, X.; Lovell, E.; Amal, R. Nitrate reduction to ammonium: from CuO defect engineering to waste NOx-to-NH3 economic feasibility. *Energy Environ. Sci.* **2021**, *14*, 3588−3598.

(8) Li, Z.; Attanayake, N. H.; Blackburn, J. L.; Miller, E. M. Carbon dioxide and nitrogen reduction reactions using 2D transition metal dichalcogenide (TMDC) and carbide/nitride (MXene) catalysts. *Energy Environ. Sci.* **2021**, *14*, 6242−6286.

(9) Andersen, S. Z.; Statt, M. J.; Bukas, V. J.; Shapel, S. G.; Pedersen, J. B.; Krempl, K.; Saccoccio, M.; Chakraborty, D.; Kibsgaard, J.; Vesborg, P. C. K.; Nørskov, J.; Chorkendorff, I. Increasing stability, efficiency, and fundamental understanding of lithium-mediated electrochemical nitrogen reduction. *Energy Environ. Sci.* **2020**, *13*, 4291−4300.

(10) McEnaney, J. M.; Blair, S. J.; Nielander, A. C.; Schwalbe, J. A.; Koshy, D. M.; Cargnello, M.; Jaramillo, T. F. Electrolyte Engineering for Efficient Electrochemical Nitrate Reduction to Ammonia on a Titanium Electrode. *ACS Sustain. Chem. Eng.* **2020**, *8*, 2672−2681.

(11) van Langevelde, P. H.; Katsounaros, I.; Koper, M. T. M. Electrocatalytic Nitrate Reduction for Sustainable Ammonia Production. *Joule* **2021**, *5*, 290−294.

(12) Liu, P.; Chen, B.; Liang, C.; Yao, W.; Cui, Y.; Hu, S.; Zou, P.; Zhang, H.; Fan, H. J.; Yang, C. Tip-Enhanced Electric Field: A New Mechanism Promoting Mass Transfer in Oxygen Evolution Reactions. *Adv. Mater.* **2021**, *33*, 2007377.

(13) Wang, Y.; Xu, A.; Wang, Z.; Huang, L.; Li, J.; Li, F.; Wicks, J.; Luo, M.; Nam, D.-H.; Tan, C.-S.; Ding, Y.; Wu, J.; Lum, Y.; Dinh, C.-T.; Sinton, D.; Zheng, G.; Sargent, E. H. Enhanced Nitrate-to-Ammonia Activity on Copper-Nickel Alloys via Tuning of Intermediate Adsorption. *J. Am. Chem. Soc.* **2020**, *142*, 5702−5708.

(14) Zhang, C.; Xu, Z.; Han, N.; Tian, Y.; Kallio, T.; Yu, C.; Jiang, L. Superaerophilic/superaerophobic cooperative electrode for efficient hydrogen evolution reaction via enhanced mass transfer. *Sci. Adv.* **2023**, *9*, No. eadd6978.

(15) Chen, F.-Y.; Wu, Z.-Y.; Gupta, S.; Rivera, D. J.; Lambeets, S. V.; Pecaut, S.; Kim, J. Y. T.; Zhu, P.; Finfrock, Y. Z.; Meira, D. M.; King, G.; Gao, G.; Xu, W.; Cullen, D. A.; Zhou, H.; Han, Y.; Perea, D. E.; Muhich, C. L.; Wang, H. Efficient conversion of low-concentration nitrate sources into ammonia on a Ru-dispersed Cu nanowire electrocatalyst. *Nat. Nanotechnol.* **2022**, *17*, 759−767.

(16) Wu, Z.-Y.; Karamad, M.; Yong, X.; Huang, Q.; Cullen, D. A.; Zhu, P.; Xia, C.; Xiao, Q.; Shakouri, M.; Chen, F.-Y.; Kim, J. Y.; Xia, Y.; Heck, K.; Hu, Y.; Wong, M. S.; Li, Q.; Gates, I.; Siahrostami, S.; Wang, H. Electrochemical ammonia synthesis via nitrate reduction on Fe single atom catalyst. *Nat. Commun.* **2021**, *12*, 2870.

(17) Fang, J.-Y.; Zheng, Q.-Z.; Lou, Y.-Y.; Zhao, K.-M.; Hu, S.-N.; Li, G.; Akdim, O.; Huang, X.-Y.; Sun, S.-G. Ampere-level current density ammonia electrochemical synthesis using CuCo nanosheets simulating nitrite reductase bifunctional nature. *Nat. Commun.* **2022**, *13*, 7899.

(18) Gao, J.; Jiang, B.; Ni, C.; Qi, Y.; Zhang, Y.; Oturan, N.; Oturan, M. A. Non-precious Co_3O_4-TiO_2/Ti cathode based electrocatalytic nitrate reduction: Preparation, performance and mechanism. *Appl. Catal., B* **2019**, *254*, 391−402.

(19) Gao, J.; Jiang, B.; Ni, C.; Qi, Y.; Bi, X. Enhanced reduction of nitrate by noble metal-free electrocatalysis on P doped three-dimensional Co_3O_4 cathode: Mechanism exploration from both experimental and DFT studies. *Chem. Eng. J.* **2020**, *382*, 123034.

(20) He, W.; Zhang, J.; Dieckhöfer, S.; Varhade, S.; Brix, A. C.; Lielpetere, A.; Seisel, S.; Junqueira, J. R. C.; Schuhmann, W. Splicing the active phases of copper/cobalt-based catalysts achieves high-rate tandem electroreduction of nitrate to ammonia. *Nat. Commun.* **2022**, *13*, 1129.

(21) Fan, K.; Xie, W.; Li, J.; Sun, Y.; Xu, P.; Tang, Y.; Li, Z.; Shao, M. Active hydrogen boosts electrochemical nitrate reduction to ammonia. *Nat. Commun.* **2022**, *13*, 7958.

(22) Shi, N.; Gao, J.; Li, K.; Li, Y.; Zhang, W.; Yang, Q.; Jiang, B. Upcycling wastewater nitrate into ammonia fertilizer via concurrent electrocatalysis and membrane extraction. *Chem. Eng. J.* **2023**, *455*, 140959.

(23) Gao, J.; Ma, Q.; Young, J.; Crittenden, J. C.; Zhang, W. Decoupling Electron- and Phase-Transfer Processes to Enhance Electrochemical Nitrate-to-Ammonia Conversion by Blending Hydrophobic PTFE Nanoparticles within the Electrocatalyst Layer. *Adv. Energy Mater.* **2023**, *13*, 2203891.

(24) Wu, X.; Nazemi, M.; Gupta, S.; Chismar, A.; Hong, K.; Jacobs, H.; Zhang, W.; Rigby, K.; Hedtke, T.; Wang, Q.; Stavitski, E.; Wong, M. S.; Muhich, C.; Kim, J.-H. Contrasting Capability of Single Atom Palladium for Thermocatalytic versus Electrocatalytic Nitrate Reduction Reaction. *ACS Catal.* **2023**, *13*, 6804−6812.

(25) Niu, Z.-Z.; Chi, L.-P.; Wu, Z.-Z.; Yang, P.-P.; Fan, M.-H.; Gao, M.-R. CO_2-assisted formation of grain boundaries for efficient CO-CO coupling on a derived Cu catalyst. *Natl. Sci. Open* **2023**, *2*, 20220044.

(26) Yu, Z.-Y.; Duan, Y.; Kong, Y.; Zhang, X.-L.; Feng, X.-Y.; Chen, Y.; Wang, H.; Yu, X.; Ma, T.; Zheng, X.; Zhu, J.; Gao, M.-R.; Yu, S.-H. General Synthesis of Tube-like Nanostructured Perovskite Oxides with Tunable Transition Metal-Oxygen Covalency for Efficient Water Electrooxidation in Neutral Media. *J. Am. Chem. Soc.* **2022**, *144*, 13163−13173.

(27) Sun, W.-J.; Ji, H.-Q.; Li, L.-X.; Zhang, H.-Y.; Wang, Z.-K.; He, J.-H.; Lu, J.-M. Built-in Electric Field Triggered Interfacial Accumulation Effect for Efficient Nitrate Removal at Ultra-Low Concentration and Electroreduction to Ammonia. *Angew. Chem., Int. Ed.* **2021**, *60*, 22933−22939.

(28) Gao, J.; Shi, N.; Guo, X.; Li, Y.; Bi, X.; Qi, Y.; Guan, J.; Jiang, B. Electrochemically Selective Ammonia Extraction from Nitrate by Coupling Electron- and Phase-Transfer Reactions at a Three-Phase Interface. *Environ. Sci. Technol.* **2021**, *55*, 10684−10694.

https://doi.org/10.1021/acsnano.4c02020
ACS Nano 2024, 18, 10302−10311

(29) Gao, J.; Shi, N.; Li, Y.; Jiang, B.; Marhaba, T.; Zhang, W. Electrocatalytic Upcycling of Nitrate Wastewater into an Ammonia Fertilizer via an Electrified Membrane. *Environ. Sci. Technol.* **2022**, *56*, 11602−11613.
(30) Hou, D.; Jassby, D.; Nerenberg, R.; Ren, Z. J. Hydrophobic Gas Transfer Membranes for Wastewater Treatment and Resource Recovery. *Environ. Sci. Technol.* **2019**, *53*, 11618−11635.
(31) Perez Sirkin, Y. A.; Gadea, E. D.; Scherlis, D. A.; Molinero, V. Mechanisms of Nucleation and Stationary States of Electrochemically Generated Nanobubbles. *J. Am. Chem. Soc.* **2019**, *141*, 10801−10811.
(32) Angulo, A.; van der Linde, P.; Gardeniers, H.; Modestino, M.; Fernández Rivas, D. Influence of Bubbles on the Energy Conversion Efficiency of Electrochemical Reactors. *Joule* **2020**, *4*, 555−579.
(33) Wakerley, D.; Lamaison, S.; Ozanam, F.; Menguy, N.; Mercier, D.; Marcus, P.; Fontecave, M.; Mougel, V. Bio-inspired hydrophobicity promotes CO_2 reduction on a Cu surface. *Nat. Mater.* **2019**, *18*, 1222−1227.
(34) Niu, Z.-Z.; Gao, F.-Y.; Zhang, X.-L.; Yang, P.-P.; Liu, R.; Chi, L.-P.; Wu, Z.-Z.; Qin, S.; Yu, X.; Gao, M.-R. Hierarchical Copper with Inherent Hydrophobicity Mitigates Electrode Flooding for High-Rate CO_2 Electroreduction to Multicarbon Products. *J. Am. Chem. Soc.* **2021**, *143*, 8011−8021.
(35) Yamauchi, Y.; Tenjimbayashi, M.; Samitsu, S.; Naito, M. Durable and Flexible Superhydrophobic Materials: Abrasion/Scratching/Slicing/Droplet Impacting/Bending/Twisting-Tolerant Composite with Porcupinefish-Like Structure. *ACS Appl. Mater. Interfaces* **2019**, *11*, 32381−32389.
(36) Liu, M.; Wang, S.; Jiang, L. Nature-inspired superwettability systems. *Nat. Rev. Mater.* **2017**, *2*, 17036.
(37) Yang, B.; Liu, K.; Li, H.; Liu, C.; Fu, J.; Li, H.; Huang, J. E.; Ou, P.; Alkayyali, T.; Cai, C.; Duan, Y.; Liu, H.; An, P.; Zhang, N.; Li, W.; Qiu, X.; Jia, C.; Hu, J.; Chai, L.; Lin, Z.; Gao, Y.; Miyauchi, M.; Cortés, E.; Maier, S. A.; Liu, M. Accelerating CO_2 Electroreduction to Multicarbon Products via Synergistic Electric-Thermal Field on Copper Nanoneedles. *J. Am. Chem. Soc.* **2022**, *144*, 3039−3049.
(38) Liu, M.; Pang, Y.; Zhang, B.; De Luna, P.; Voznyy, O.; Xu, J.; Zheng, X.; Dinh, C. T.; Fan, F.; Cao, C.; de Arquer, F. P. G.; Safaei, T. S.; Mepham, A.; Klinkova, A.; Kumacheva, E.; Filleter, T.; Sinton, D.; Kelley, S. O.; Sargent, E. H. Enhanced electrocatalytic CO_2 reduction via field-induced reagent concentration. *Nature* **2016**, *537*, 382−386.
(39) Huo, Z.-Y.; Winter, L. R.; Wang, X.-X.; Du, Y.; Wu, Y.-H.; Hübner, U.; Hu, H.-Y.; Elimelech, M. Synergistic Nanowire-Enhanced Electroporation and Electrochlorination for Highly Efficient Water Disinfection. *Environ. Sci. Technol.* **2022**, *56*, 10925−10934.
(40) Wang, T.; Brown, D. K.; Xie, X. Operando Investigation of Locally Enhanced Electric Field Treatment (LEEFT) Harnessing Lightning-Rod Effect for Rapid Bacteria Inactivation. *Nano Lett.* **2022**, *22*, 860−867.
(41) Jin, C. Y.; Li, Z.; Williams, R. S.; Lee, K. C.; Park, I. Localized Temperature and Chemical Reaction Control in Nanoscale Space by Nanowire Array. *Nano Lett.* **2011**, *11*, 4818−4825.
(42) Gao, F.-Y.; Hu, S.-J.; Zhang, X.-L.; Zheng, Y.-R.; Wang, H.-J.; Niu, Z.-Z.; Yang, P.-P.; Bao, R.-C.; Ma, T.; Dang, Z.; Guan, Y.; Zheng, X.-S.; Zheng, X.; Zhu, J.-F.; Gao, M.-R.; Yu, S.-H. High-Curvature Transition-Metal Chalcogenide Nanostructures with a Pronounced Proximity Effect Enable Fast and Selective CO_2 Electroreduction. *Angew. Chem., Int. Ed.* **2020**, *59*, 8706−8712.
(43) DuanMu, J.-W.; Gao, M.-R. Advances in bio-inspired electrocatalysts for clean energy future. *Nano Res.* **2024**, *17*, 515−533.
(44) Liu, G.; Wong, W. S.; Kraft, M.; Ager, J. W.; Vollmer, D.; Xu, R. Wetting-regulated gas-involving (photo) electrocatalysis: biomimetics in energy conversion. *Chem. Soc. Rev.* **2021**, *50*, 10674−10699.
(45) Kiros, Y.; Bursell, M. Low Energy Consumption in Chlor-alkali Cells Using Oxygen Reduction Electrodes. *Int. J. Electrochem. Sci.* **2008**, *3*, 444−451.
(46) Xing, Z.; Hu, L.; Ripatti, D. S.; Hu, X.; Feng, X. Enhancing carbon dioxide gas-diffusion electrolysis by creating a hydrophobic catalyst microenvironment. *Nat. Commun.* **2021**, *12*, 136.
(47) Lyu, Z.; Zhu, S.; Xie, M.; Zhang, Y.; Chen, Z.; Chen, R.; Tian, M.; Chi, M.; Shao, M.; Xia, Y. Controlling the Surface Oxidation of Cu Nanowires Improves Their Catalytic Selectivity and Stability toward C_{2+} Products in CO_2 Reduction. *Angew. Chem., Int. Ed.* **2021**, *60*, 1909−1915.
(48) Zhou, J.; Pan, F.; Yao, Q.; Zhu, Y.; Ma, H.; Niu, J.; Xie, J. Achieving efficient and stable electrochemical nitrate removal by in-situ reconstruction of Cu_2O/Cu electroactive nanocatalysts on Cu foam. *Appl. Catal., B* **2022**, *317*, 121811.
(49) Chen, G.-F.; Yuan, Y.; Jiang, H.; Ren, S.-Y.; Ding, L.-X.; Ma, L.; Wu, T.; Lu, J.; Wang, H. Electrochemical reduction of nitrate to ammonia via direct eight-electron transfer using a copper-molecular solid catalyst. *Nat. Energy* **2020**, *5*, 605−613.
(50) Liu, D.; Li, X.; Chen, S.; Yan, H.; Wang, C.; Wu, C.; Haleem, Y. A.; Duan, S.; Lu, J.; Ge, B.; Ajayan, P. M.; Luo, Y.; Jiang, J.; Song, L. Atomically dispersed platinum supported on curved carbon supports for efficient electrocatalytic hydrogen evolution. *Nat. Energy* **2019**, *4*, 512−518.
(51) Wang, T.; Xie, X. Nanosecond bacteria inactivation realized by locally enhanced electric field treatment. *Nat. Water* **2023**, *1*, 104−112.
(52) Möller, T.; Ngo Thanh, T.; Wang, X.; Ju, W.; Jovanov, Z.; Strasser, P. The product selectivity zones in gas diffusion electrodes during the electrocatalytic reduction of CO_2. *Energy Environ. Sci.* **2021**, *14*, 5995−6006.
(53) Liang, C.; Zou, P.; Nairan, A.; Zhang, Y.; Liu, J.; Liu, K.; Hu, S.; Kang, F.; Fan, H. J.; Yang, C. Exceptional performance of hierarchical Ni-Fe oxyhydroxide@NiFe alloy nanowire array electrocatalysts for large current density water splitting. *Energy Environ. Sci.* **2020**, *13*, 86−95.
(54) Zouch, H.; Cabrol, L.; Chifflet, S.; Tedetti, M.; Karray, F.; Zaghden, H.; Sayadi, S.; Quéméneur, M. Effect of acidic industrial effluent release on microbial diversity and trace metal dynamics during resuspension of coastal sediment. *Front. Microbiol.* **2018**, *9*, 3103.
(55) Dhamole, P. B.; Nair, R. R.; D'Souza, S. F.; Lele, S. Denitrification of highly alkaline nitrate waste using adapted sludge. *Appl. Biochem. Biotechnol.* **2008**, *151*, 433−440.
(56) Zheng, W.; Zhu, L.; Yan, Z.; Lin, Z.; Lei, Z.; Zhang, Y.; Xu, H.; Dang, Z.; Wei, C.; Feng, C. Self-Activated Ni Cathode for Electrocatalytic Nitrate Reduction to Ammonia: From Fundamentals to Scale-Up for Treatment of Industrial Wastewater. *Environ. Sci. Technol.* **2021**, *55*, 13231−13243.
(57) Huo, X.; Vanneste, J.; Cath, T. Y.; Strathmann, T. J. A hybrid catalytic hydrogenation/membrane distillation process for nitrogen resource recovery from nitrate-contaminated waste ion exchange brine. *Water Res.* **2020**, *175*, 115688.
(58) Zhu, Z.; Zhong, L.; Horseman, T.; Liu, Z.; Zeng, G.; Li, Z.; Lin, S.; Wang, W. Superhydrophobic-omniphobic membrane with anti-deformable pores for membrane distillation with excellent wetting resistance. *J. Membr. Sci.* **2021**, *620*, 118768.
(59) Kim, D. J.; Gao, Y.; Rigby, K.; Meese, A. F.; Lim, H. J.; Wang, H.; Kim, J. H.; Kim, J.-H. Pulsed Electrolysis of Boron-Doped Carbon Dramatically Improves Impurity Tolerance and Longevity of H_2O_2 Production. *Environ. Sci. Technol.* **2023**, *57*, 7309−7320.
(60) Yang, Y.; Hoffmann, M. R. Synthesis and Stabilization of Blue-Black TiO_2 Nanotube Arrays for Electrochemical Oxidant Generation and Wastewater Treatment. *Environ. Sci. Technol.* **2016**, *50*, 11888−11894.
(61) Wang, Y.; Li, Y.; Liu, J.; Dong, C.; Xiao, C.; Cheng, L.; Jiang, H.; Jiang, H.; Li, C. $BiPO_4$-Derived 2D Nanosheets for Efficient Electrocatalytic Reduction of CO_2 to Liquid Fuel. *Angew. Chem., Int. Ed.* **2021**, *133*, 7759−7763.
(62) Liu, C.; Qian, J.; Ye, Y.; Zhou, H.; Sun, C.-J.; Sheehan, C.; Zhang, Z.; Wan, G.; Liu, Y.-S.; Guo, J.; Li, S.; Shin, H.; Hwang, S.; Gunnoe, T. B.; Goddard, W. A.; Zhang, S. Oxygen evolution reaction over catalytic single-site Co in a well-defined brookite TiO_2 nanorod surface. *Nat. Catal.* **2021**, *4*, 36−45.

https://doi.org/10.1021/acsnano.4c02020
ACS Nano 2024, 18, 10302−10311